Journal of Neuroscience Methods 414 (2025) 110320

Contents lists available at ScienceDirect

Journal of Neuroscience Methods

journal homepage: www.elsevier.com/locate/jneumeth

Improving computational models of deep brain stimulation through experimental calibration

Jan Philipp Payonk [a,*], Henning Bathel [a], Nils Arbeiter [a], Maria Kober [b], Mareike Fauser [b], Alexander Storch [b,c], Ursula van Rienen [a,d,e], Julius Zimmermann [a,1]

[a] Institute of General Electrical Engineering, University of Rostock, Albert-Einstein-Straße 2, Rostock, 18051, Germany
[b] Department of Neurology, University of Rostock, Gehlsheimer Straße 20, Rostock, 18147, Germany
[c] German Centre for Neurodegenerative Diseases (DZNE) Rostock-Greifswald, Gehlsheimer Straße 20, Rostock, 18147, Germany
[d] Department Life, Light & Matter, University of Rostock, Albert-Einstein-Straße 25, Rostock, 18051, Germany
[e] Department of Ageing of Individuals and Society, University of Rostock, Albert-Einstein-Straße 21, Rostock, 18051, Germany

ARTICLE INFO

Dataset link: https://doi.org/10.5281/zenodo.14179720

Keywords:
Computational modeling
Deep brain stimulation
Impedance spectroscopy
Encapsulation tissue
Dielectric properties
Uncertainty quantification

ABSTRACT

Background: Deep brain stimulation has become a well-established clinical tool to treat movement disorders. Nevertheless, the knowledge of processes initiated by the stimulation remains limited. To address this knowledge gap, computational models are developed to gain deeper insight. However, their predictive power remains constrained by model uncertainties and a lack of validation and calibration.
New method: Exemplified with rodent microelectrodes, we present a workflow for validating electrode model geometry using microscopy and impedance spectroscopy *in vitro* before implantation. We address uncertainties in the tissue distribution and dielectric properties and outline a concept for calibrating the computational model based on *in vivo* impedance spectroscopy measurements.
Results: The standard deviation of the volume of tissue activated across the 18 characterized electrodes was approximately 32.93%, underscoring the importance of electrode characterization. Thus, the workflow significantly enhances the model predictions' credibility of neural activation exemplified in a rodent model.
Comparison with existing methods: Computational models are frequently employed without validation or calibration, relying instead on manufacturers' specifications. Our approach provides an accessible method to obtain a validated and calibrated electrode geometry, which significantly enhances the reliability of the computational model that relies on this electrode.
Conclusion: By reducing the uncertainties of the model, the accuracy in predicting neural activation is increased. The entire workflow is realized in open-source software, making it adaptable for other use cases, such as deep brain stimulation in humans. Additionally, the framework allows for the integration of further experiments, enabling live updates and refinements to computational models.

1. Introduction

Deep brain stimulation (DBS) has emerged as a widely used treatment for various neurological disorders, in particular for movement disorders such as Parkinson's disease (PD) (Deuschl et al., 2006). While improvements of PD motor symptoms are often observed within minutes to a few days (Castaño-Candamil et al., 2019), DBS effects in dystonia are far more delayed (Kupsch et al., 2006). Likewise, its efficacy for diseases primarily characterized by non-motor symptoms, such as depression, anxiety, and Alzheimer's disease, is the subject of ongoing research (Kisely et al., 2018; Laxton et al., 2010). Currently, the major roadblock preventing optimized patient-specific stimulation protocols is the limited understanding of the mechanisms of action. This applies in particular when immediate responses are not observable. In this context, it is crucial to consider all potential uncertainties in DBS applications. An accurately manufactured electrode plays a key role, particularly in experiments using custom-made electrodes, where manufacturing uncertainties are often not considered.

To better understand these mechanisms and to refine DBS applications, rodent models are widely employed to study its use in treating various diseases and developing new therapeutic approaches. For example, the use of DBS for PD has been investigated in rats (Campos et al., 2020; Ruiz et al., 2022; Fauser et al., 2024), DBS for dystonia

* Corresponding author.
E-mail addresses: jan.payonk@uni-rostock.de (J.P. Payonk), ursula.van-rienen@uni-rostock.de (U. van Rienen).
[1] Now with: Synthetic Physiology Lab, Department of Civil Engineering and Architecture, University of Pavia, Pavia, Italy

https://doi.org/10.1016/j.jneumeth.2024.110320
Received 13 August 2024; Received in revised form 20 October 2024; Accepted 6 November 2024
Available online 15 November 2024

in hamsters (Lüttig et al., 2024), the regulation of inflammation in mice (Falvey et al., 2024). Further examples can be found in Zhang et al. (2024). Due to the size of the rodent's brain, customized electrodes are usually used, introducing an additional source of uncertainty. However, a consistent evaluation of the impact of uncertainties of the electrode geometry is usually not conducted. While the electrode geometry can be straightforwardly integrated into numerical models and its impact on the field distribution in the brain can be elucidated (Gimsa et al., 2006), it has not yet become common practice to use experimentally validated geometries in the models neither in humans nor in rodents.

Computational models play a pivotal role in refining the understanding of the mechanism of interaction in DBS. By predicting stimulation outcomes, the models shall unravel the underlying mechanics of DBS. Advanced biophysical models and neuroimaging methods have unlocked patient-specific computational models (Butenko et al., 2020; Neudorfer et al., 2023). Yet, the models rely on many assumptions and are usually not validated against experimental data. Hence, their reliability and predictive power are limited. The main challenge towards validation is the limited accessibility of the stimulation system before and after implantation. Thus, relatively simple methods have to be used. For example, the impedance at 1 kHz is often considered a quality control measure for stimulation electrodes, despite neglecting the strong frequency dependence of the impedance, which can lead to changes in orders of magnitude (Evers et al., 2022).

In this work, we suggest a combination of microscopy and impedance spectroscopy to implement a validated geometry model of the stimulation electrodes. We investigated microelectrodes for DBS in rodents in an *in vitro* setting. Consequently, we established a volume conductor model (VCM) in a rat model to simulate the electric field and volume of tissue activated (VTA) during DBS. Our results suggest that using single frequency measurements as a quality control is not sufficient because it cannot capture deviations of the geometry from the manufacturer's specifications. Indeed, the geometrical uncertainty significantly impacts the predicted electric field and VTA and needs to be considered.

A second aspect is model calibration, as the electrochemical properties of the stimulation electrodes and the tissue around the electrode can change during the stimulation (Gimsa et al., 2005; Lempka et al., 2009). In rats, for example, an encapsulation layer forms shortly after implantation and significantly affects the impedance (Badstübner et al., 2017). We present a concept to extract the properties of the encapsulation layer during stimulation by combining impedance measurements and the numerical model. Eventually, the goal is to realize a computational model that is informed continuously during the stimulation.

In sum, we present how to enhance the fidelity of the model by validating the stimulation electrode geometry in a controlled *in vitro* setting. Then, we outline how this concept can be translated to the *in vivo* condition. The approach is general and can be straightforwardly adapted to human DBS. As we base all our analysis exclusively on open-source software, it can be readily employed by other researchers.

2. Methods

2.1. Electrode characterization by microscopy

We used 40 custom-designed monopolar platinum DBS electrodes (Microprobes for Life Science, Gaithersburg, USA) (see Fig. 1). According to the manufacturer's specifications, the electrodes have a lead radius of 112.50 µm, which is equivalent to the radius of the exposed rounded tip serving as the stimulation contact, and a 1.5 µm-thick polyamide coating. A Keyence VHX-5000 digital microscope with a VH-Z100UR/W/T lens (Keyence Corporation, Osaka, Japan) was used to take images of the electrodes. The geometric parameters were extracted from the microscope images to estimate their variability. We employed OpenTurns (Baudin et al., 2015) to fit parametric distribution functions for each measured value of the geometrical parameters.

2.2. In vitro characterization

We conducted impedance spectroscopy to electrochemically characterize the electrodes. The electrodes were immersed in a tank filled with electrolyte solution. A gold wire was placed in the tank and served as the ground because the used electrodes were monopolar. The wire was placed 1 cm away from the electrode (see Fig. 1E). We used a KCl electrolyte solution (1413 µS cm^{-1} at 25 °C, HANNA instruments, Woonsocket, USA) and a physiological NaCl solution (15 550 µS cm^{-1} at 25 °C, B. Braun SE, Melsungen, Germany). During measurements, the temperature of the solution was 20 °C, and the corresponding conductivities were computed based on the manufacturer specification to be 1278 µS cm^{-1} for KCl and 13 995 µS cm^{-1} for NaCl. Impedance spectroscopy was performed on 20 out of the 40 electrodes, utilizing KCl and NaCl solutions. The impedance spectroscopy was performed with a Sciospec ISX-3 impedance analyzer (Sciospec Scientific Instruments, Bennewitz, Germany). We swept the frequency logarithmically from 100 Hz to 10 MHz and measured the impedance at 100 points per decade (600 points in total) at a peak amplitude of 50 mV. We chose the internal measurement range `100OHM`, and each frequency point was averaged 10 times by the impedance analyzer to reduce noise.

2.3. Impedance fitting

Following the *in vitro* measurements, the acquired data was fitted to an equivalent circuit model using the *ImpedanceFitter* software library (Zimmermann and Thiele, 2021). The equivalent circuit utilized for fitting (Fig. 1F) includes a lead resistance R_{OSI} and a lead inductance L_{OSI}, which represents the OSI SCL-0.7-130 cables connecting the electrode to the power source. OSI cables are wound-up stainless steel wires (provided by Open Source Instruments Inc., Waltham, USA). Additionally, the circuit incorporates a constant phase element Z_{CPE} in parallel with a resistor R_{ct}. The solution is modeled as a pure resistance R_{sol}, while a stray capacitance C_{stray} is introduced to account for the capacitive effects in the experimental setup.

The impedance characteristics of the OSI cables were measured separately. A 15 cm piece was measured with a Novocontrol NEISYS impedance analyzer (Novocontrol Technologies, Montabaur, Germany) using an input voltage of 14 mV$_{\mathrm{RMS}}$ and frequencies from 1 Hz to 100 MHz at 20 points per decade. The line resistance R_{OSI} was 5.89 Ω cm^{-1} and the line inductance L_{OSI} was 51.25 nH cm^{-1}. The electrode and gold wire were connected to the measurement device by two cables with a total length of 30 cm. Hence, a fixed value of 176.7 Ω was used for the lead resistance, and a fixed value of 1.54 µH was used for the lead inductance.

2.4. Computational modeling

A geometric and numerical model was constructed to represent the electrode's characterization in the known homogeneous medium. A 3D model of the experimental geometry was created and meshed using the open-source software NGSolve (Schöberl, 2014) with the integrated meshing module from Netgen (Schöberl, 1997). The finite element method, as implemented in NGSolve, was employed to solve for the electric potential φ from the electro-quasistatic (EQS) formulation of Maxwell's equations

$$\nabla \cdot ((\sigma + j\omega\varepsilon)\,\nabla\varphi) = 0\,. \tag{1}$$

Here, j denotes the imaginary unit, ω is the angular frequency, σ represents the conductivity, and ε denotes the permittivity of the medium. The electric field $\mathbf{E}$ is the negative gradient of the electric potential in this formulation. The impedance of the simulated system was computed as described in Zimmermann et al. (2021). Unless otherwise stated, we used second-order curved finite elements.

To model the *in vitro* setup, it is sufficient to consider only Laplace's equation as the modeling domain comprises only one material (a more

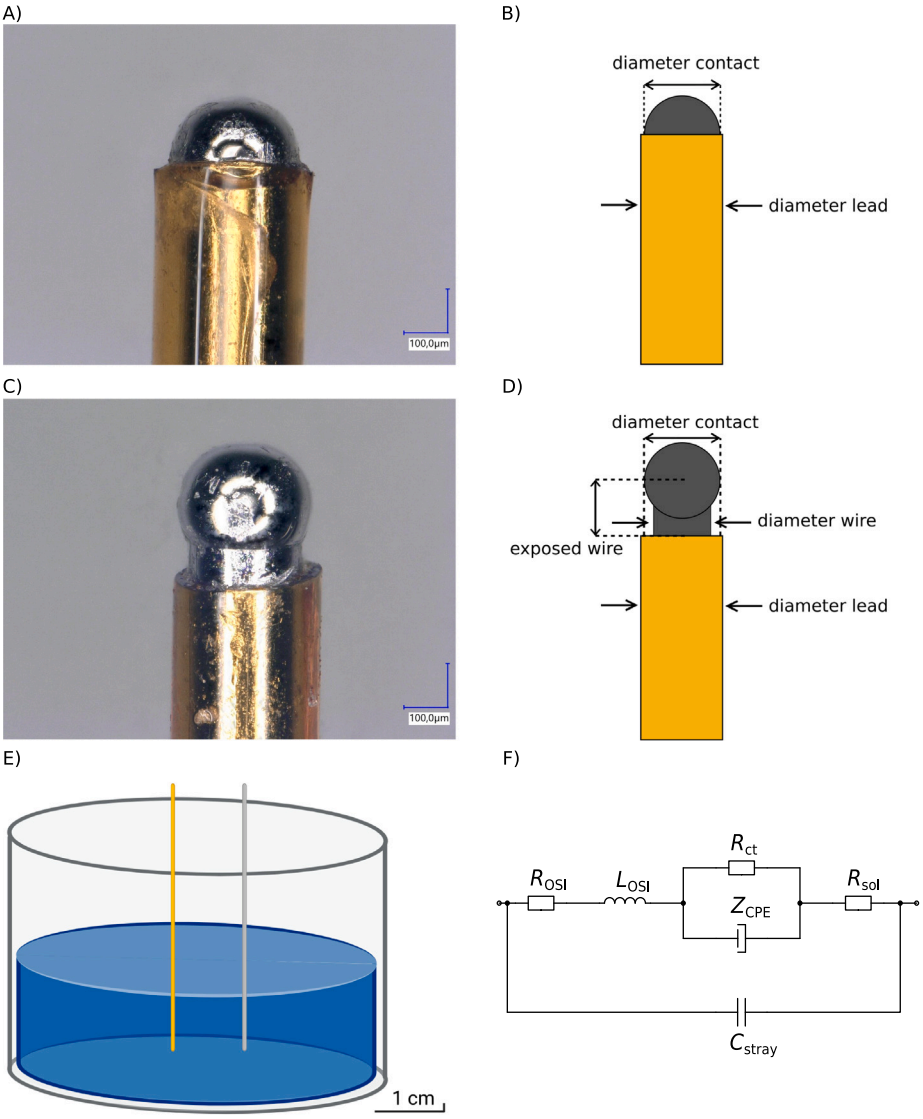

Fig. 1. Microscope images and schematic perspectives of the investigated monopolar microelectrode (A–D) and the related experimental setup (E) with circuit model (F). (A, B) Electrode with a half-sphere as the rounded tip, as specified by the manufacturer. The electrode features a platinum wire entirely enclosed in the polyamide tubing. (C, D) Electrode with an extended exposed part of the platinum wire, increasing the contact surface area. (E) Schematic design of the *in vitro* experiment with the electrode and an unshielded gold wire used as counterelectrode. (F) Equivalent circuit model for the *in vitro* characterization of the electrode, encompassing circuit elements representing the used OSI cables, the electrolyte solution, and the electrode with its interface to the solution.

detailed discussion is provided in Zimmermann et al. (2021)). In this case, only the resistance instead of the impedance was computed.

We created a full rat head model to study the effect of DBS on rodents. The model was based on the usual electrode placement in rodent DBS of the subthalamic nucleus with monopolar electrodes. In this case, a gold wire is placed close to the electrode lead and acts as the counter electrode (Plocksties et al., 2021). Thus, we modeled a patch on the top of the brain as a ground contact instead of grounding the entire brain surface. In preliminary simulations, we found differences in the impedance between the two configurations and chose the more realistic geometry. An encapsulation layer forming around the electrode was modeled with a 100 µm thickness as in previous works on rodents (Butenko et al., 2019).

Eq. (1) was solved, and the impedance was computed across a broad frequency range from 100 Hz to 10 MHz, which comprises all relevant frequencies of the spectrum of standard DBS pulses (Butenko et al., 2019). All computations were performed with a stimulation amplitude of 1 V. However, due to the linearity of the electro-quasistatic field equation, the results can be scaled according to the amplitude. The *in vivo* simulations were carried out using our open-source framework OSS-DBSv2[2], which is based on NGSolve.

When simulating *in vivo* studies in rats, we considered the tissue's inhomogeneous and dispersive nature (Butenko et al., 2020). To represent the inhomogeneous distribution of white matter (WM), gray matter (GM), and cerebrospinal fluid (CSF) in the brain, a segmented image from a multi-contrast MR atlas of the Wistar rat brain was utilized (Johnson et al., 2021). The choice of the dielectric properties is not straightforward because of the large variation of the brain properties (McCann et al., 2019). The four dispersions Cole–Cole model

[2] https://github.com/SFB-ELAINE/OSS-DBSv2

Table 1
Dielectric parameters of the Cole–Cole model. Minimum and maximum values for gray matter, white matter, and blood of each parameter are given. The high-frequency limit of the relative permittivity $\varepsilon_\infty = 4$ remained constant.

Dielectric parameters of the Cole–Cole model		
Parameters	Minimum values	Maximum values
$\alpha_1, \ldots, \alpha_4$	(0.1, 0.0, 0.0, 0.0)	(0.1, 0.15, 0.3, 0.02)
$\Delta\varepsilon_1, \ldots, \Delta\varepsilon_4$	(32.0, 40.0, 0.0, 0.0)	(65.0, 5200.0, 2.0×10^5, 4.5×10^7)
σ	0.02	0.7
$\tau_1, \ldots, \tau_4$	(7.96×10^{-12}, 1.592×10^{-9}, 0.0, 0.0)	(8.38×10^{-12}, 132.63×10^{-9}, 106.103×10^{-6}, 7.958×10^{-3})

(CC4) introduced by Gabriel et al. is often used (Gabriel et al., 1996). We recently found that the CC4 model may contain electrode-specific contributions and suggested using only the three dispersions Cole–Cole model (CC3) (Zimmermann and van Rienen, 2021). A comparison between the CC3 and CC4 models for the relevant tissue types is shown in the supplementary information (SI) Sec. S3-E. To account for the electrode–tissue interface, the fitted parameters of the CPE were used to approximate the interface in the *in vivo* setup by an equivalent-circuit approach (Zimmermann et al., 2023).

To test the convergence of the computational model, we computed the impedance spectrum using different mesh qualities (see Figure S5). We compared the results to the case where the maximum element size was set equal to the voxel size because this setting marks the optimal case for the given image resolution. The model was assumed to converge when the difference in the estimated impedance was below 0.5 % at all frequencies.

2.5. Uncertainty quantification

To assess the impact of varying geometrical properties of the electrode on stimulation outcomes, we conducted uncertainty quantification (UQ) (Tennøe et al., 2018). In UQ, sets of parameter combinations are drawn from probability distributions describing the individual parameters and their uncertainty. An efficient opportunity to reduce the number of parameter combinations is to use polynomial chaos, which evaluates the model at selected parameter combinations and creates a surrogate model containing information about the parameters' uncertainty. The polynomial chaos expansion yields statistical quantities such as the mean and standard deviation (SD). In addition, the Sobol' indices of first and total order are obtained, which reveal the impact of individual parameters on the model result. Other quantities, such as the 5th and 95th percentile, are obtained from sampling the surrogate model. We defined the prediction interval as the range between the 5th and 95th percentile (i.e., it is the 90 % prediction interval). We used the Python library Uncertainpy (Tennøe et al., 2018) with the default settings (polynomial chaos expansion method with 4th-order polynomials and 10^4 samples drawn from the surrogate model).

Further, we conducted a UQ for the dielectric properties of an encapsulation layer forming around the electrode within the *in vivo* setup (Schmidt et al., 2016). Each parameter of the CC4 model was assumed to vary uniformly within the minimal and maximal values range across GM, WM, and blood (see Table 1).

2.6. Volume of tissue activated estimate

To assess the effect of the DBS in the rat model, we considered the volume of tissue activated (VTA) (Butenko and van Rienen, 2022). In this study, we employed a thresholding technique to compute the VTA based on values reported by Åström et al. Åström et al. (2014). As the fiber diameter in rats is comparably small, we use the value for activating fibers with a diameter of 2.0 µm. Consequently, we apply a threshold of 0.371 V mm^{-1} for 1 V amplitude and 60 µs pulse width stimulation (refer to Table 3 in Åström et al. (2014)) to our calculated electric field. For the thresholding approach, we only considered the solution at a frequency of 10 kHz.

3. Results

In the following, we present the key results of our workflow. First, the properties of the real electrode geometry are investigated using microscopy and impedance spectroscopy, followed by the construction of a virtual electrode geometry for use in computational simulations. Then, we proceed to *in vivo* models and highlight the impact of the electrode geometry as well as the influence of encapsulation tissue on the VTA size. Finally, we discuss how the model could be calibrated during *in vivo* stimulation.

3.1. Electrode characterization by microscopy

We observed significant deviations between the electrode geometries measured in the microscope images and the manufacturer's specifications. The mean radius of the rounded tip was 37.82 % larger than expected. Likewise, the mean radius of the electrode lead was about 47.81 % larger than stated. Some electrodes featured an exposed wire below the rounded tip, which in turn increased the total active contact surface. We found a high variation, especially in the length of the exposed part (see Fig. 1). The distribution of the measured values is summarized in Table 2 (see also Figure S4).

We used the Lilliefors goodness-of-fit test to find distributions that fit the sample best (Lilliefors, 1967). Among the tested distributions, the beta distribution yielded the best results. We report it in the form of B(α, β, [a, b]), where α and β represent the distribution parameters, and [a, b] denotes the interval of the distribution (see Table 2 and Fig. 3).

3.2. Comparing experimental and computational results

The impedance spectra show characteristic behavior: interface impedance is dominant at low frequencies, and inductive effects due to the cables play a role only at high frequencies (see SI S2-A). We can extract the characteristic resistance (R_{sol} in Fig. 1F) by fitting and comparing it to the simulated impedance (see Figure S1). We observed a noticeable offset in the impedance when comparing the experimental data with the simulated resistance (see Figure S1). The mean resistance was 5816.38 Ω based on the fits from all experimentally characterized electrodes. The simulated impedance, based on manufacturer data, was 7874.94 Ω, and therefore 35.39% larger than expected. To test if the offset resulted from the assumed electrode geometry based on manufacturer data, we used the actual geometry of each electrode as observed under the microscope. This refinement resulted in a significant improvement in the agreement between the simulation and experimental results in both considered electrolyte solutions (results in KCl are shown in Fig. 2, results in NaCl in Figure S3). In the following, we considered only the KCl solution as its conductivity is closer to the brain tissue conductivity. Two out of 20 electrodes had a relative error above 10 %. Because the geometrical properties could not explain such a high deviation, those electrodes were assumed to be damaged and were not used for further stimulation experiments.

3.3. Uncertainty quantification

We used the probability distributions obtained from microscopy to estimate the uncertainty of the computational model. The mean impedance as obtained by the UQ was 5486.55 Ω with a standard deviation of 515.93 Ω. The 90 % prediction interval ranged from 4715.39 Ω to 6412.26 Ω.

The first-order Sobol' indices, as a measure of sensitivity, suggest that the tip radius significantly impacts the total impedance, while the length of the exposed wire demonstrates a minor effect (see Fig. 3). Further, the radius of the electrode lead exhibits minimal impact on the estimated results. These findings emphasize the crucial role of an accurately manufactured tip while the tubing does not need to ideally insulate the remaining part of the electrode. We also considered

Table 2
Geometrical parameters of the measured electrodes and parameters for fitted beta distribution. The ideal values are shown with the characterized mean values and standard deviations (n = 40).

Electrode parameters			Fitted beta distribution		
Electrode parameters (μm)	Ideal electrode	Measured (mean ± SD)	α	β	[a, b]
Tip radius	112.50	155.04 ± 9.94	1.78	1.98	[134.2, 178.2]
Lead radius	114.00	168.50 ± 4.25	2.12	0.98	[155.67, 174.42]
Exposed wire	0.00	38.17 ± 37.90	1.51	2.79	[−26.80, 158.21]

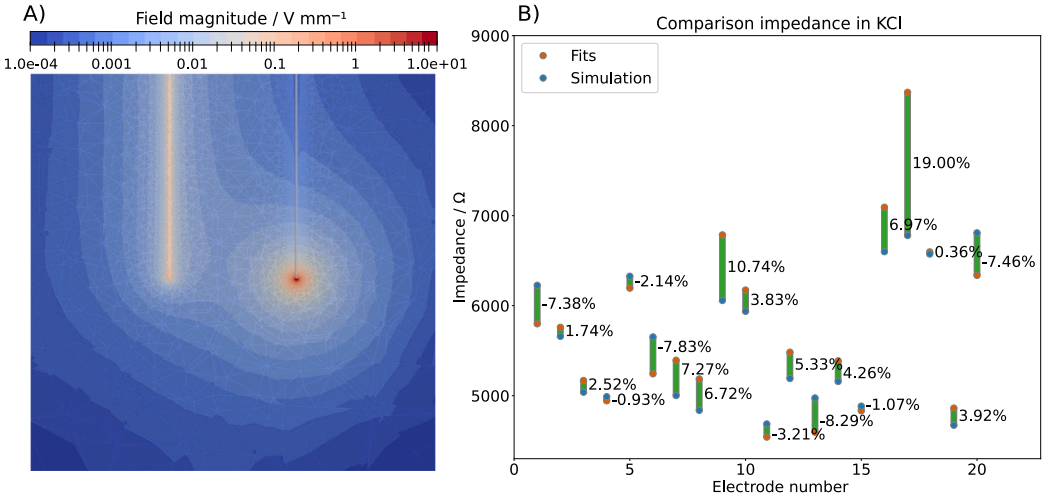

Fig. 2. Simulation results for *in vitro* characterization in KCl. (A) The magnitude of the electric field in the *in vitro* experiment is shown for a monopolar electrode placed 1 cm from an uninsulated, grounded gold wire. (B) The comparison of experimentally determined impedance with computationally estimated resistance R_{sol} in KCl is shown. The error bars represent the difference between both results for each electrode. Likewise, the relative difference is shown.

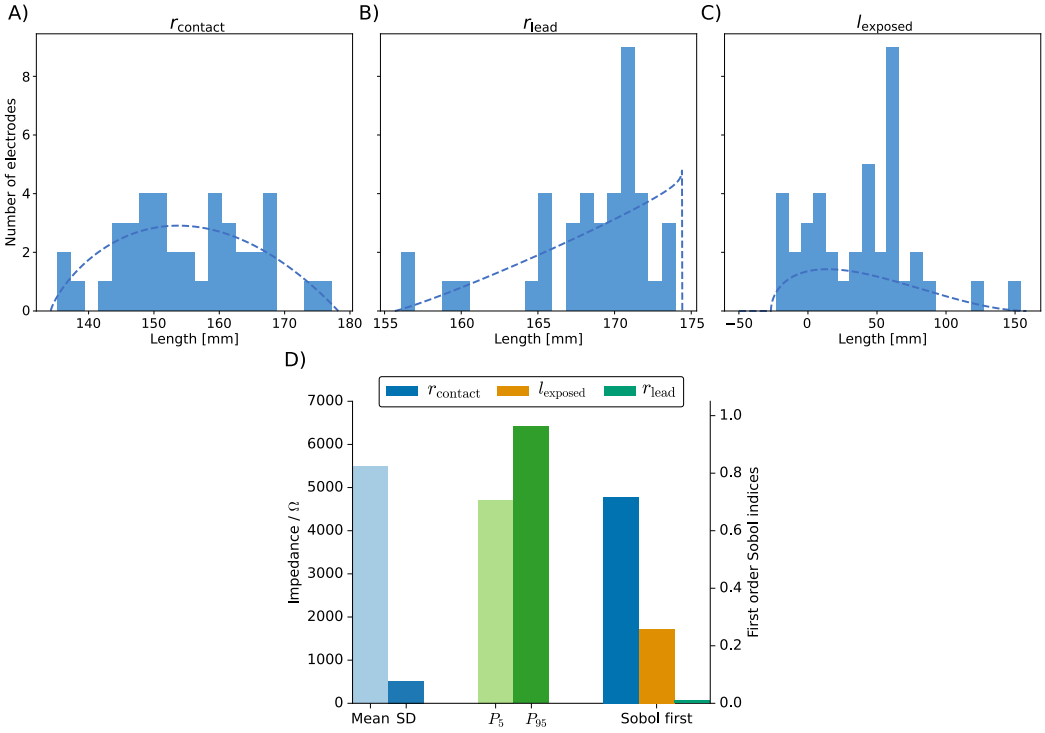

Fig. 3. Sensitivity analysis on geometrical parameters of the DBS electrode in the *in vitro* setup. In the upper panel (A–C), a histogram of the geometrical parameters is shown together with the fitted beta distribution described in Table 2. Since the number of electrodes ($n = 40$) allows considering alternative distributions, further simulations are shown in SI S3.1, leading to comparable results. (D) The mean value and the standard deviation (SD) for the impedance, as well as the 5th and the 95th percentile, are shown. Additionally, the first-order Sobol' indices, which indicate the parameter sensitivity for the uncertain parameters such as the contact radius $r_{contact}$, the length of the exposed part $l_{exposed}$, and the lead radius r_{lead}, are presented.

distributions other than the beta distribution including the normal distribution and two uniform distributions with different support (see SI S3.1). The difference in the estimated mean value was less than 8.2%, and the difference in the 5th and the 95th percentile was less than 5.7%.

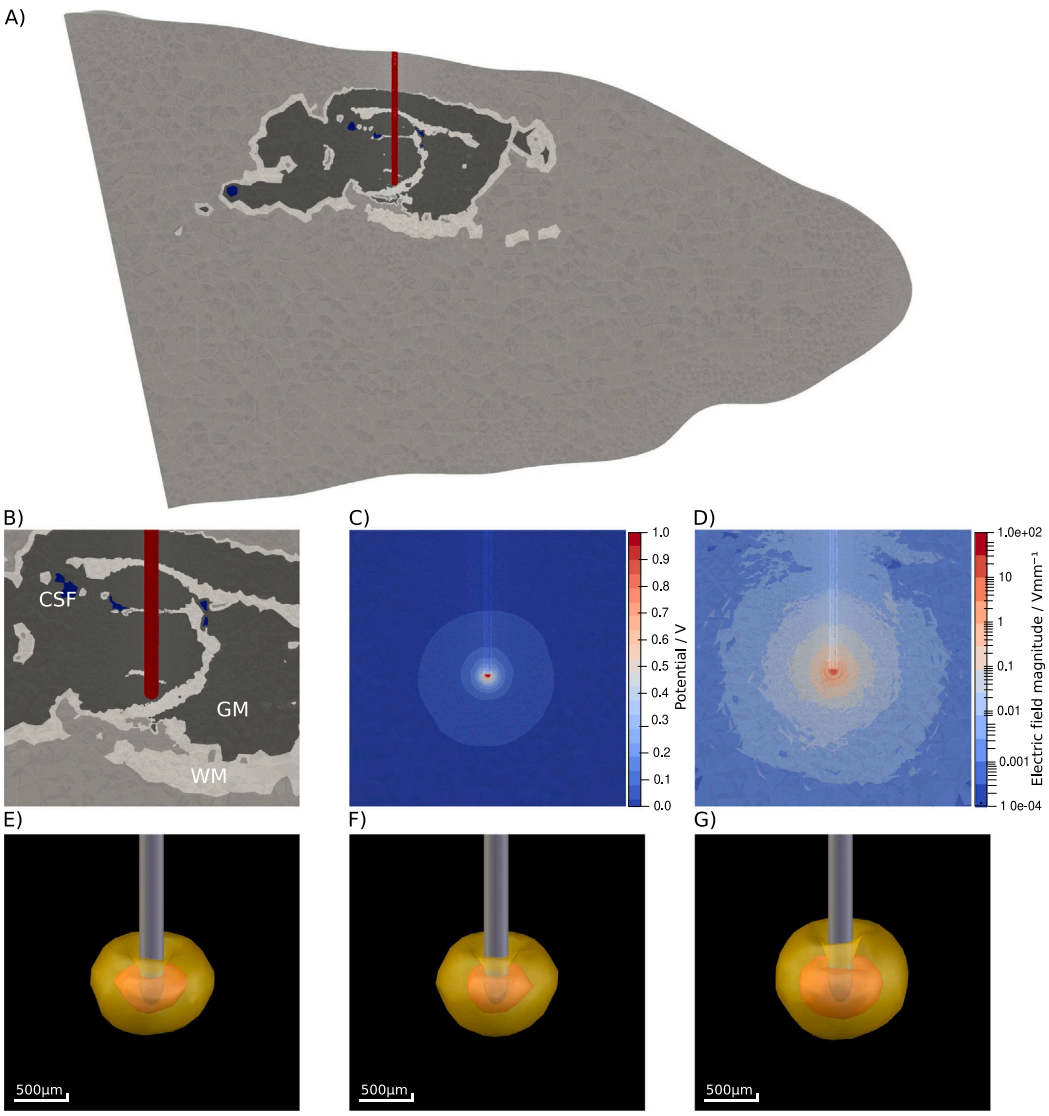

Fig. 4. Computational model of the rat head. (A) Sagittal section of the full 3D rat head model used in the simulations. (B–D) Close-up view of the inhomogeneous material distribution in the model, including gray matter (GM), white matter (WM), cerebrospinal fluid (CSF), and the electrode with its surrounding encapsulation layer (B). Potential distribution (C) and magnitude of the electric field (D) during unit 1 V stimulation at a frequency of 10 kHz. (E–G) Simulation results of the volume of tissue activated (VTA) without encapsulation layer ((E) - 0.133 mm^3 versus 0.613 mm^3), with 100 µm layer of gray matter ((F) - 0.137 mm^3 versus 0.593 mm^3) and with 100 µm layer of blood ((G) - 0.201 mm^3 versus 0.815 mm^3). Results are presented for the electrode generating the smallest VTAs (orange) and the electrode generating the largest VTAs (yellow).

This result underscores the robustness of the UQ result. The first-order Sobol' indices show that the impact of the lead radius r_{lead} is negligible for all modeled distributions.

3.4. Translation to in vivo studies

The geometry models of the 18 validated electrodes were used to model DBS in a full rat head model incorporating gray matter, white matter, and cerebrospinal fluid (Andree et al., 2022). Thus, we accounted for the deviations in the electrode geometry to obtain a reliable numerical model. Furthermore, the thickness of the encapsulation layer was set to 100 µm, and it was modeled as gray matter. The CC3 model, which assumes the brain to be predominantly characterized by resistance (Logothetis et al., 2007; Zimmermann and van Rienen, 2021), was used to model the dielectric properties.

An exemplary electric field distribution in the brain for a single electrode is shown in Fig. 4. Because the potential around the electrode decays quickly and the electric field vanishes (see Fig. 4), we cropped the computational domain. The validity of the model reduction has been tested by comparing the impedance of the reduced model to the impedance of the full model. Further visual comparisons can be found in Figure S6.

The electrode-specific VTAs obtained by thresholding the electric field magnitude at 0.371 $V\,mm^{-1}$ revealed considerable variations in size. The mean VTA size was 0.353 mm^3 with a standard deviation of 0.116 mm^3, corresponding to a variation of 32.93 %. Notably, the largest estimated VTA reached 0.593 mm^3, while the smallest volume was estimated at 0.137 mm^3.

3.4.1. Impact of encapsulation tissue

After validating the geometrical model of the electrode, the tissue surrounding the electrode is the main source of uncertainty. Here, we assumed that the MRI image provides sufficient information about the brain and only studied the impact of the encapsulation layer on the impedance and the size of the VTA. For that, we initially focused on the impact of the dielectric properties of the encapsulation layer.

In the first scenario, we assumed that the encapsulation layer has the same properties as gray matter, which represents the most common tissue type in the brain. In the second scenario, the encapsulation layer was assumed to be filled with blood, which has a significantly higher

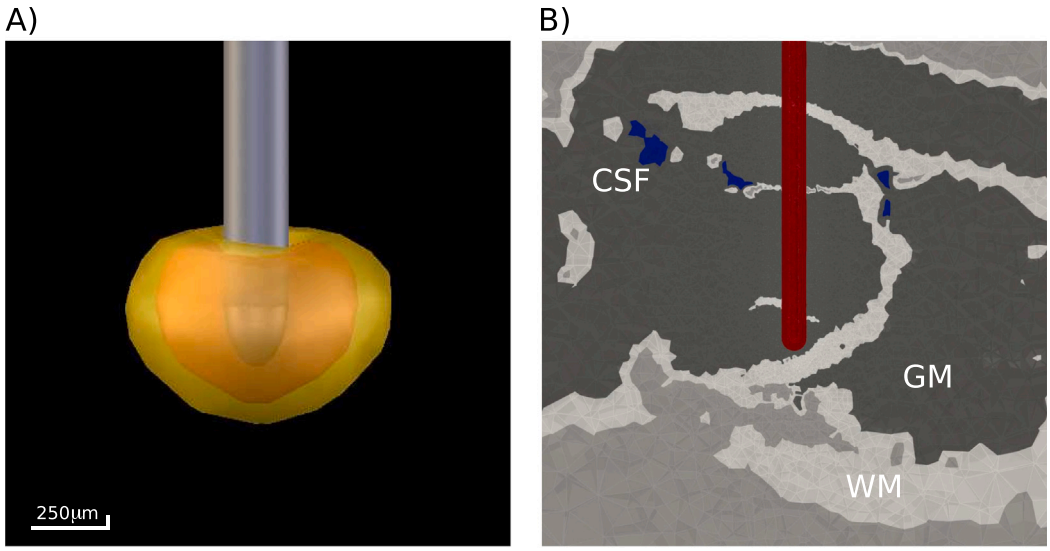

Fig. 5. Visualization of the VTA using two different models of the dielectric properties. (A) The VTA is shown for a simulation using the three-dispersion Cole–Cole model (orange) compared to the four-dispersion Cole–Cole model (yellow) for the electrode with the median VTA size. (B) The material distribution affects the shape of the VTA, especially in the four-dispersion Cole–Cole model, which has lower conductivity, resulting in a larger VTA.

conductivity than gray and white matter. This scenario represents the acute case shortly after the electrode implantation (Polikov et al., 2005; Grill and Thomas Mortimer, 1994). The impact of the dielectric properties on the VTA is significant: in the case of the high conductivity (blood), the VTA is, on average, 30.17% larger, with a maximum difference of 53.18 % (see Fig. 4). The corresponding impedance spectra (see Figure S7) show a significant change as well, as the impedance at 10 kHz is almost halved.

Using the CC4 model with the electrode-specific approximation of the interface effects instead would lead to a 10 % larger mean VTA size (see Fig. 5). Significant spectra changes can also be observed (see SI S9). Eventually, we wanted to probe if the total impedance is sufficient to simultaneously identify both dielectric properties and geometrical parameters. This means testing if the impedance spectrum can be described by only one encapsulation layer thickness, one permittivity, and one conductivity. If this is not the case, either the dielectric properties (permittivity and conductivity) or the thickness of the encapsulation layer have to be known to extract these parameters reliably from an impedance spectrum.

First, we determined which parameters contribute mainly to the uncertainty of the impedance of the entire brain tissue (see Fig. 6). As the conductivity of the encapsulation tissue has the largest impact on the impedance, we focused solely on this parameter. We estimated the encapsulation thickness so that the impedance for different choices of σ matches 5701.187 Ω, which is the impedance for a 100.00 µm thick encapsulation layer with gray matter properties and a conductivity of 0.15 S m^{-1} at 10 kHz. We found that conductivities of 0.1 S m^{-1}, 0.15 S m^{-1}, and 0.2 S m^{-1} yielded the desired impedance with corresponding encapsulation thicknesses of 284.64 µm, 100.00 µm, and 69.39 µm. This demonstrates that either the dielectric properties or the thickness of the encapsulation layer have to be known to extract the other quantity from the impedance spectrum. If both are unknown, no unique solution exists to the inverse problem.

4. Discussion

In DBS research, realistic simulation models are crucial to understand the underlying mechanism and developing optimized stimulation schemes. To date, numerical models of DBS electric field distributions rely on multiple assumptions on the geometry and material properties, which carry significant uncertainties (Neudorfer et al., 2023). Here, we focused on the uncertainty of the electrode geometry. While electrodes for human DBS (e.g., commercially available electrodes for clinical use or custom-made electrodes used in preclinical studies) carry manufacturing uncertainties, the geometric uncertainties of electrodes for use in rodent models can be expected to be particularly significant. The higher uncertainties are caused by the need for miniaturization compared to human DBS electrodes because of the smaller brain size. However, the geometry of custom-made electrodes is usually not analyzed in detail and is also not considered in computational models.

The electrode geometry is a key ingredient when building a patient-specific computational DBS model. Usually, the electrode geometry is chosen based on manufacturer specifications or reconstruction algorithms (Neudorfer et al., 2023). Both approaches introduce geometrical uncertainties. This is particularly relevant when only manufacturer specifications are available because the manufacturing accuracy needs to be accounted for. Because the electrode geometry is not accessible after implantation, we developed an *in vitro* characterization workflow. We employed a comprehensive approach combining microscopy, impedance spectroscopy, and computational simulations to account for uncertainties in geometrical parameters and validate electrode characteristics. Recently, guidelines for standardized performance tests for electrodes intended for neural interfaces have been introduced, which focus only on electrochemical characterization (Boehler et al., 2020). Our approach goes beyond these guidelines as the numerical simulations enable us to formulate an initial expectation and permit us to update the model of the electrode geometry. Thus, we can distinguish usable but slightly deformed electrodes from damaged electrodes. In addition, we have shown that the geometrical uncertainties of the stimulation electrodes significantly impact the VTA, i.e., the stimulation targeting. This adds to UQ studies that have mainly considered electrochemical electrode properties or tissue properties (Butson et al., 2006; Schmidt and van Rienen, 2013). A key advantage of our simulation pipeline is the straightforward update of electrode geometries, which enables fast and automated UQ studies.

As our suggested experimental characterization does not require elevated resources, it can, in principle, be conducted before every stimulation experiment. As a result, realistic model geometries are used in the numerical model, which enhances its reliability compared to models relying solely on manufacturer specifications. The simplicity of the *in vitro* approach facilitates a transfer to other electrodes and stimulation settings. In this study, for example, we adjusted *in vivo* models based on

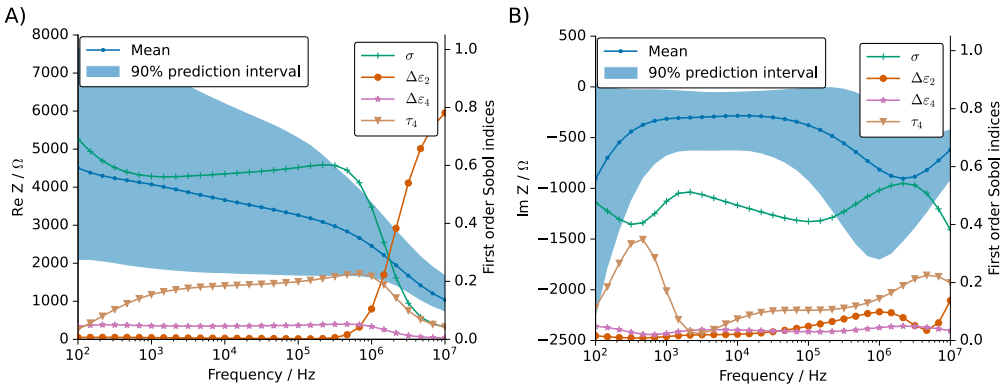

Fig. 6. Frequency-dependent first-order Sobol' indices for selected parameters of the four-dispersion Cole–Cole model along with the mean values and 90 % prediction intervals for (A) the real and (B) the imaginary parts of the impedance over a wide frequency range. We use the ideal electrode geometry, and the dielectric properties of the encapsulation layer were estimated based on the four-dispersion Cole–Cole model. We varied a selection of parameters from the model to observe their impact, including the conductivity σ, the magnitude of the 2nd and 4th dispersion $\Delta\varepsilon_2$, $\Delta\varepsilon_4$, and the mean relaxation time of the 4th dispersion τ_4. As indicated by the frequency-dependent first-order Sobol' indices, the conductivity has the largest impact on the estimated impedance, except for the real part of the impedance in the megahertz range, which is most sensitive to the magnitude of the second dispersion.

the *in vitro* characterization to mitigate uncertainties in the electrode geometry. While recent studies have explored brain stimulation in rodents (Lüttig et al., 2024; Falvey et al., 2024), simulations have yet to be conducted. With our approach, reliable field strength estimates will become accessible.

Yet, *in vitro* characterization cannot account for processes during the stimulation. It has been shown that the impedance changes during stimulation because of changes in the encapsulation tissue (Lempka et al., 2009), but also due to stimulation-induced changes in the electrode–tissue interface (Evers et al., 2022). These stimulation-induced changes have been observed to result from protein absorption and desorption at the electrode. They are mostly reversible, and cessation or resumption of stimulation increases or decreases impedance, respectively (Evers et al., 2022). Here, we used parameters for the electrochemical interface as determined in the *in vitro* characterization. This approximation most likely does not fully reflect the *in vivo* situation and cannot account for dynamic processes at the electrode–tissue interface.

Besides the geometrical and electrochemical properties of the electrode, the tissue properties around the electrode significantly impact the stimulation outcomes (Butson et al., 2006; Butson and McIntyre, 2005). As we have shown, the accumulation of blood (or other highly conductive liquids) within the encapsulation tissue can be expected to lead to a much larger VTA. Thus, the stimulation in the chronic state differs from the initial state, in which scar tissue forms around the electrode. These changes in the encapsulation tissue have been characterized using impedance spectroscopy (Lempka et al., 2009). We also observed significant changes in the impedance estimated through the stimulation electrode when altering the encapsulation tissue properties. Thus, we wanted to investigate if impedance spectroscopy could help to simultaneously detect changes in the dielectric properties or the thickness of the encapsulation layer. However, we have shown that this is not possible. The inverse problem, determining the dielectric properties and thickness of the encapsulation layer, is ambiguous, and one parameter can only be extracted from the impedance if the other one is known.

Another source of uncertainty is the choice of the dielectric properties. Usually, an empirical model based on data from the literature is used, the CC4 model (Gabriel et al., 1996). The CC4 model incorporates resistive and capacitive effects, potentially including electrode-specific interface interactions, which eventually lead to low conductivity values that are not in agreement with other conductivity measurements (Zimmermann and van Rienen, 2021). As the CC4 model may contain complex electrode–tissue interactions specific to the originally used electrode, it may not be consistent with the experimental data of our electrodes. In contrast, the CC3 model incorporates the tissue's resistive properties and excludes these inherent interface effects through an algorithmic correction of the CC4 model. Thus, it enables us to add an electrode-specific model of electrode–tissue interactions based on our *in vitro* impedance spectroscopy data. By integrating our experimental data rather than relying on predefined assumptions, the CC3 model allows for a more accurate representation of electrochemical interface effects. Still, our approach relies on the assumption that the electrochemical interface properties obtained *in vitro* can be assumed during *in vivo* stimulation. However, this assumption needs to be scrutinized through *in vivo* investigations (Lempka et al., 2009).

A comprehensive understanding of the electrode–tissue interface is essential to reduce uncertainties in modeling. Characterizing the interface during the stimulation is challenging (Evers et al., 2022). While impedance measurements can indirectly reflect changes at the electrode–tissue interface, accurately interpreting these measurements requires a thorough understanding and characterization of all factors affecting the impedance. Our theoretical results indicate that ideally, the size of the encapsulation layer is known from external measurements to gain access to electrochemical and dielectric properties. Ideally, validation measurements can be conducted during the stimulation to better link the electrical stimulation to the clinical effect. Simultaneous recordings of voltage and current transients could help to estimate the impedance during the stimulation (Zimmermann et al., 2021) and update the numerical model.

Additionally, a feedback loop with reliable VTA or pathway activation models could be developed (Parastarfeizabadi and Kouzani, 2017). In this work, we employed a simple estimate of the VTA to predict stimulation outcomes instead of more sophisticated methods such as pathway activation modeling (Butenko and van Rienen, 2022). While using the volume of the VTA as a measure of changes in the stimulation outcome, the percent activation of specific pathways would be assessed based on pathway activation modeling (PAM). However, performing precise pathway activation modeling in rodents is challenging because no detailed normative connectomes are available.

Uncertainties in the electrode geometry can also occur in electrodes for human DBS. Yet, detailed information on manufacturing tolerances is scarce, and the high cost of human DBS electrodes limits the ability to conduct a thorough investigation, as introduced in this work for rodent electrodes. However, all simulations were carried out using a modular and easily adaptable platform to facilitate similar future model extensions. This modularity ensures that our modeling approach can be re-used to simulate DBS in humans. Furthermore, translation to more complex measures such as PAM, is straightforward, as they are mostly based on the estimated potential distribution.

5. Conclusion

Our study highlights the importance of accurately characterizing electrode properties and understanding the uncertainties associated with DBS modeling. Through a comprehensive approach combining experimental characterization and computational modeling, we demonstrated the significant impact of geometrical variations on stimulation outcomes. Furthermore, our use of open-source modeling frameworks emphasizes the accessibility and applicability of our approach for future research in DBS, both in humans and in different rodent disease models. While we focused on immediate changes due to geometrical variations, future studies should consider longitudinal effects at the electrode–tissue interface to refine our understanding further. Overall, our work advances the precision and reliability of DBS modeling for more accurate predictions of stimulation outcomes and improved pre-clinical and clinical applications.

CRediT authorship contribution statement

Jan Philipp Payonk: Writing – original draft, Visualization, Validation, Software, Methodology, Formal analysis. **Henning Bathel:** Writing – review & editing, Investigation, Data curation. **Nils Arbeiter:** Writing – review & editing, Investigation, Data curation. **Maria Kober:** Resources, Investigation, Data curation. **Mareike Fauser:** Writing – review & editing, Resources, Funding acquisition. **Alexander Storch:** Writing – review & editing, Supervision, Resources, Funding acquisition. **Ursula van Rienen:** Writing – review & editing, Supervision, Resources, Funding acquisition. **Julius Zimmermann:** Writing – original draft, Validation, Supervision, Software, Methodology, Conceptualization.

Declaration of competing interest

None.

Acknowledgment

This work is funded by the Deutsche Forschungsgemeinschaft (DFG, German Research Foundation) - SFB 1270/2 – 299150580.

Appendix A. Supplementary data

Supplementary material related to this article can be found online at https://doi.org/10.1016/j.jneumeth.2024.110320.

Data availability

The data has been deposited on Zenodo https://doi.org/10.5281/zenodo.14179720.

References

Andree, A., Li, N., Butenko, K., Kober, M., Chen, J.Z., Higuchi, T., Fauser, M., Storch, A., Ip, C.W., Kühn, A.A., et al., 2022. Deep brain stimulation electrode modeling in rats. Exp. Neurol. 350, 113978. http://dx.doi.org/10.1016/j.expneurol.2022.113978.

Åström, M., Diczfalusy, E., Martens, H., Wårdell, K., 2014. Relationship between neural activation and electric field distribution during deep brain stimulation. IEEE Trans. Biomed. Eng. 62 (2), 664–672. http://dx.doi.org/10.1109/TBME.2014.2363494.

Badstübner, K., Stubbe, M., Kröger, T., Mix, E., Gimsa, J., 2017. Impedance detection of the electrical resistivity of the wound tissue around deep brain stimulation electrodes permits registration of the encapsulation process in a rat model. J. Electr. Bioimpedance 8 (1), 11–24. http://dx.doi.org/10.5617/jeb.4086.

Baudin, M., Dutfoy, A., Iooss, B., Popelin, A.-L., 2015. Open TURNS: An industrial software for uncertainty quantification in simulation. arXiv preprint arXiv:1501.05242.

Boehler, C., Carli, S., Fadiga, L., Stieglitz, T., Asplund, M., 2020. Tutorial: guidelines for standardized performance tests for electrodes intended for neural interfaces and bioelectronics. Nat. Protoc. 15 (11), 3557–3578. http://dx.doi.org/10.1038/s41596-020-0389-2.

Butenko, K., Bahls, C., van Rienen, U., 2019. Evaluation of epistemic uncertainties for bipolar deep brain stimulation in rodent models. In: 2019 41st Annual International Conference of the IEEE Engineering in Medicine and Biology Society. EMBC, IEEE, pp. 2136–2140. http://dx.doi.org/10.1109/EMBC.2019.8857910.

Butenko, K., Bahls, C., Schröder, M., Köhling, R., van Rienen, U., 2020. OSS-DBS: Open-source simulation platform for deep brain stimulation with a comprehensive automated modeling. PLoS Comput. Biol. 16 (7), e1008023. http://dx.doi.org/10.1371/journal.pcbi.1008023.

Butenko, K., van Rienen, U., 2022. Chapter 7 - DBS imaging methods III: Estimating the electric field and volume of tissue activated. In: Horn, A. (Ed.), Connectomic Deep Brain Stimulation. Academic Press, pp. 147–168. http://dx.doi.org/10.1016/B978-0-12-821861-7.00021-X.

Butson, C.R., Maks, C.B., McIntyre, C.C., 2006. Sources and effects of electrode impedance during deep brain stimulation. Clin. Neurophysiol. 117 (2), 447–454. http://dx.doi.org/10.1016/j.clinph.2005.10.007.

Butson, C.R., McIntyre, C.C., 2005. Role of electrode design on the volume of tissue activated during deep brain stimulation. J. Neural Eng. 3 (1), 1. http://dx.doi.org/10.1088/1741-2560/3/1/001.

Campos, A.C.P., Kikuchi, D.S., Paschoa, A.F.N., Kuroki, M.A., Fonoff, E.T., Hamani, C., Pagano, R.L., Hernandes, M.S., 2020. Unraveling the role of astrocytes in subthalamic nucleus deep brain stimulation in a Parkinson's disease rat model. Cell. Mol. Neurobiol. 40, 939–954. http://dx.doi.org/10.1007/s10571-019-00784-3.

Castaño-Candamil, S., Piroth, T., Reinacher, P., Sajonz, B., Coenen, V.A., Tangermann, M., 2019. An easy-to-use and fast assessment of patient-specific DBS-induced changes in hand motor control in Parkinson's disease. IEEE Trans. Neural Syst. Rehabil. Eng. 27 (10), 2155–2163. http://dx.doi.org/10.1109/TNSRE.2019.2941453.

Deuschl, G., Schade-Brittinger, C., Krack, P., Volkmann, J., Schäfer, H., Bötzel, K., Daniels, C., Deutschländer, A., Dillmann, U., Eisner, W., et al., 2006. A randomized trial of deep-brain stimulation for parkinson's disease. N. Engl. J. Med. 355 (9), 896–908. http://dx.doi.org/10.1056/NEJMoa060281.

Evers, J., Sridhar, K., Liegey, J., Brady, J., Jahns, H., Lowery, M., 2022. Stimulation-induced changes at the electrode-tissue interface and their influence on deep brain stimulation. J. Neural Eng. 19 (4), 046004. http://dx.doi.org/10.1088/1741-2552/ac7ad6.

Falvey, A., Palandira, S.P., Chavan, S.S., Brines, M., Dantzer, R., Tracey, K.J., Pavlov, V.A., 2024. Electrical stimulation of the dorsal motor nucleus of the vagus in male mice can regulate inflammation without affecting the heart rate. Brain Behav. Immun. http://dx.doi.org/10.1016/j.bbi.2024.04.027.

Fauser, M., Payonk, J.P., Weber, H., Statz, M., Winter, C., Hadar, R., Appali, R., van Rienen, U., Brandt, M.D., Storch, A., 2024. Subthalamic nucleus but not entopeduncular nucleus deep brain stimulation enhances neurogenesis in the SVZ-olfactory bulb system of Parkinsonian rats. Front. Cell. Neurosci. 18, 1396780. http://dx.doi.org/10.3389/fncel.2024.1396780.

Gabriel, S., Lau, R., Gabriel, C., 1996. The dielectric properties of biological tissues: III. Parametric models for the dielectric spectrum of tissues. Phys. Med. Biol. 41 (11), 2271. http://dx.doi.org/10.1088/0031-9155/41/11/003.

Gimsa, J., Habel, B., Schreiber, U., van Rienen, U., Strauss, U., Gimsa, U., 2005. Choosing electrodes for deep brain stimulation experiments–electrochemical considerations. J. Neurosci. Methods 142 (2), 251–265. http://dx.doi.org/10.1016/j.jneumeth.2004.09.001.

Gimsa, U., Schreiber, U., Habel, B., Flehr, J., van Rienen, U., Gimsa, J., 2006. Matching geometry and stimulation parameters of electrodes for deep brain stimulation experiments—Numerical considerations. J. Neurosci. Methods 150 (2), 212–227. http://dx.doi.org/10.1016/j.jneumeth.2005.06.013.

Grill, W.M., Thomas Mortimer, J., 1994. Electrical properties of implant encapsulation tissue. Ann. Biomed. Eng. 22, 23–33. http://dx.doi.org/10.1007/BF02368219.

Johnson, G.A., Laoprasert, R., Anderson, R.J., Cofer, G., Cook, J., Pratson, F., White, L.E., 2021. A multicontrast MR atlas of the Wistar rat brain. NeuroImage 242, 118470. http://dx.doi.org/10.1016/j.neuroimage.2021.118470.

Kisely, S., Li, A., Warren, N., Siskind, D., 2018. A systematic review and meta-analysis of deep brain stimulation for depression. Depress. Anxiety 35 (5), 468–480. http://dx.doi.org/10.1002/da.22746.

Kupsch, A., Benecke, R., Müller, J., Trottenberg, T., Schneider, G.-H., Poewe, W., Eisner, W., Wolters, A., Müller, J.-U., Deuschl, G., et al., 2006. Pallidal deep-brain stimulation in primary generalized or segmental dystonia. N. Engl. J. Med. 355 (19), 1978–1990. http://dx.doi.org/10.1056/NEJMoa063618.

Laxton, A.W., Tang-Wai, D.F., McAndrews, M.P., Zumsteg, D., Wennberg, R., Keren, R., Wherrett, J., Naglie, G., Hamani, C., Smith, G.S., et al., 2010. A phase 1 trial of deep brain stimulation of memory circuits in Alzheimer's disease. Ann. Neurol. 68 (4), 521–534. http://dx.doi.org/10.1002/ana.22089.

Lempka, S.F., Miocinovic, S., Johnson, M.D., Vitek, J.L., McIntyre, C.C., 2009. In vivo impedance spectroscopy of deep brain stimulation electrodes. J. Neural Eng. 6 (4), 046001. http://dx.doi.org/10.1088/1741-2560/6/4/046001.

Lilliefors, H.W., 1967. On the Kolmogorov-Smirnov test for normality with mean and variance unknown. J. Amer. Statist. Assoc. 62 (318), 399–402. http://dx.doi.org/10.1080/01621459.1967.10482916.

Logothetis, N.K., Kayser, C., Oeltermann, A., 2007. In vivo measurement of cortical impedance spectrum in monkeys: implications for signal propagation. Neuron 55 (5), 809–823. http://dx.doi.org/10.1016/j.neuron.2007.07.027.

Lüttig, A., Perl, S., Zetsche, M., Richter, F., Franz, D., Heerdegen, M., Köhling, R., Richter, A., 2024. Short-term stimulations of the entopeduncular nucleus induce cerebellar changes of c-Fos expression in an animal model of paroxysmal dystonia. Brain Res. 1823, 148672. http://dx.doi.org/10.1016/j.brainres.2023.148672.

McCann, H., Pisano, G., Beltrachini, L., 2019. Variation in reported human head tissue electrical conductivity values. Brain Topogr. 32 (5), 825–858. http://dx.doi.org/10.1007/s10548-019-00710-2.

Neudorfer, C., Butenko, K., Oxenford, S., Rajamani, N., Achtzehn, J., Goede, L., Hollunder, B., Ríos, A.S., Hart, L., Tasserie, J., et al., 2023. Lead-DBS v3.0: Mapping deep brain stimulation effects to local anatomy and global networks. NeuroImage 268, 119862. http://dx.doi.org/10.1016/j.neuroimage.2023.119862.

Parastarfeizabadi, M., Kouzani, A.Z., 2017. Advances in closed-loop deep brain stimulation devices. J. Neuroeng. Rehabil. 14, 1–20. http://dx.doi.org/10.1186/s12984-017-0295-1.

Plocksties, F., Kober, M., Niemann, C., Heller, J., Fauser, M., Nüssel, M., Uster, F., Franz, D., Zwar, M., Lüttig, A., et al., 2021. The software defined implantable modular platform (STELLA) for preclinical deep brain stimulation research in rodents. J. Neural Eng. 18 (5), 056032. http://dx.doi.org/10.1088/1741-2552/ac23e1.

Polikov, V.S., Tresco, P.A., Reichert, W.M., 2005. Response of brain tissue to chronically implanted neural electrodes. J. Neurosci. Methods 148 (1), 1–18. http://dx.doi.org/10.1016/j.jneumeth.2005.08.015.

Ruiz, M.C.M., Guimarães, R.P., Mortari, M.R., 2022. Parkinson's disease rodent models: Are they suitable for DBS research? J. Neurosci. Methods 380, 109687. http://dx.doi.org/10.1016/j.jneumeth.2022.109687.

Schmidt, C., Dunn, E., Lowery, M., van Rienen, U., 2016. Uncertainty quantification of oscillation suppression during DBS in a coupled finite element and network model. IEEE Trans. Neural Syst. Rehabil. Eng. 26 (2), 281–290. http://dx.doi.org/10.1109/TNSRE.2016.2608925.

Schmidt, C., van Rienen, U., 2013. Modelling the probabilistic neural activation in deep brain stimulation: Influence of uncertainty in the parameters of the electrode-tissue-interface. In: 2013 International Symposium on Electromagnetic Theory. IEEE, pp. 365–368.

Schöberl, J., 1997. NETGEN an advancing front 2D/3D-mesh generator based on abstract rules. Comput. Vis. Sci. 1 (1), 41–52. http://dx.doi.org/10.1007/s007910050004.

Schöberl, J., 2014. C++ 11 Implementation of Finite Elements in NGSolve. Tech. Rep., ASC-2014-30, Institute for Analysis and Scientific Computing.

Tennøe, S., Halnes, G., Einevoll, G.T., 2018. Uncertainpy: a python toolbox for uncertainty quantification and sensitivity analysis in computational neuroscience. Front. Neuroinform. 12, 49. http://dx.doi.org/10.3389/fninf.2018.00049.

Zhang, K.K., Matin, R., Gorodetsky, C., Ibrahim, G.M., Gouveia, F.V., 2024. Systematic review of rodent studies of deep brain stimulation for the treatment of neurological, developmental and neuropsychiatric disorders. Transl. Psychiatry 14 (1), 186. http://dx.doi.org/10.1038/s41398-023-02727-5.

Zimmermann, J., Budde, K., Arbeiter, N., Molina, F., Storch, A., Uhrmacher, A.M., van Rienen, U., 2021. Using a digital twin of an electrical stimulation device to monitor and control the electrical stimulation of cells in vitro. Front. Bioeng. Biotechnol. 9, 765516. http://dx.doi.org/10.3389/fbioe.2021.765516.

Zimmermann, J., van Rienen, U., 2021. Ambiguity in the interpretation of the low-frequency dielectric properties of biological tissues. Bioelectrochemistry 140, 107773. http://dx.doi.org/10.1016/j.bioelechem.2021.107773.

Zimmermann, J., Sahm, F., Arbeiter, N., Bathel, H., Song, Z., Bader, R., Jonitz-Heincke, A., van Rienen, U., 2023. Experimental and numerical methods to ensure comprehensible and replicable alternating current electrical stimulation experiments. Bioelectrochemistry 151, 108395. http://dx.doi.org/10.1016/j.bioelechem.2023.108395.

Zimmermann, J., Thiele, L., 2021. j-zimmermann/ImpedanceFitter: v2.0.2. http://dx.doi.org/10.5281/zenodo.5116618.